Structured Dendritic Inhibition Supports Branch-Selective Integration in CA1 Pyramidal Cells

Highlights

- Cell-type-specific inhibitory connectivity measured using array tomography

- Precise synaptic targeting to dendritic branch types and sub-branch compartments

- Functional implications examined with computational modeling

- Spatially targeted patterns of inhibition shape dendritic integration

Authors

Erik B. Bloss, Mark S. Cembrowski, Bill Karsh, Jennifer Colonell, Richard D. Fetter, Nelson Spruston

Correspondence

sprustonn@janelia.hhmi.org

In Brief

Using large-volume array tomography, Bloss et al. demonstrate that cell-type-specific targeting of inhibitory synapses onto pyramidal cell dendrites is remarkably precise. Structured patterns of connectivity enable cell-type-specific control over synaptic integration as well as initiation and backpropagation of action potentials.

CrossMark

CellPress

Structured Dendritic Inhibition Supports Branch-Selective Integration in CA1 Pyramidal Cells

Erik B. Bloss,[1] Mark S. Cembrowski,[1] Bill Karsh,[1] Jennifer Colonell,[1] Richard D. Fetter,[1] and Nelson Spruston[1],*
[1]Janelia Research Campus, Howard Hughes Medical Institute, Ashburn, VA 20147, USA
*Correspondence: sprustonn@janelia.hhmi.org
http://dx.doi.org/10.1016/j.neuron.2016.01.029

SUMMARY

Neuronal circuit function is governed by precise patterns of connectivity between specialized groups of neurons. The diversity of GABAergic interneurons is a hallmark of cortical circuits, yet little is known about their targeting to individual postsynaptic dendrites. We examined synaptic connectivity between molecularly defined inhibitory interneurons and CA1 pyramidal cell dendrites using correlative light-electron microscopy and large-volume array tomography. We show that interneurons can be highly selective in their connectivity to specific dendritic branch types and, furthermore, exhibit precisely targeted connectivity to the origin or end of individual branches. Computational simulations indicate that the observed subcellular targeting enables control over the nonlinear integration of synaptic input or the initiation and backpropagation of action potentials in a branch-selective manner. Our results demonstrate that connectivity between interneurons and pyramidal cell dendrites is more precise and spatially segregated than previously appreciated, which may be a critical determinant of how inhibition shapes dendritic computation.

INTRODUCTION

The neural mechanisms underlying cognition are understood as a series of input-output transformations performed across highly specialized neural circuits. The complexity of these transformations reflects the remarkable diversity of cell types and the specific manner in which they are interconnected within each circuit. Structured forms of connectivity are most evident between distinct cell types (Brown and Hestrin, 2009; Pfeffer et al., 2013; Yoshimura and Callaway, 2005), although it has become increasingly clear that synaptic connectivity can also be structured at progressively finer spatial scales onto the postsynaptic dendritic arbor of many neuron types (Druckmann et al., 2014; Kleindienst et al., 2011; Petreanu et al., 2009; Takahashi et al., 2012).

The passive and active properties of the dendritic tree provide a biophysical substrate for spatially structured input patterns to drive specific computations in individual neurons (Spruston, 2008). The branched morphology strongly compartmentalizes the effect of dendritic inhibitory synapses, for example, rendering their effects branch specific (Gidon and Segev, 2012; Hao et al., 2009; Koch et al., 1983; Müllner et al., 2015). Moreover, at the sub-branch level, inhibition placed proximally (i.e., near the branch origin) or distally (i.e., near the branch end) can elicit different effects on dendritic integration due to location-specific differences in the biophysical properties of dendrites and their interactions with synaptic and voltage-sensitive conductances (Gidon and Segev, 2012; Jadi et al., 2012). These functional effects suggest that precise dendritic targeting could be an effective way for specific inhibitory synapses to differentially control synaptic integration.

CA1 pyramidal cells are the primary output neurons of the hippocampus; they receive synaptic excitation from distinct afferent pathways targeting the proximal and distal domains of the dendritic arbor. Dendritic excitation is countered by inhibition from local interneuron cell types that differ widely in their gene expression, morphology, connectivity, and physiology (Klausberger and Somogyi, 2008). The majority of these cell types provide synaptic inhibition targeted to specific domains of the dendritic tree, often matching the spatial distribution of the afferent excitatory pathways (Klausberger, 2009). Such an arrangement is intriguing, as it suggests that specific inhibitory cell types provide pathway-selective control over the input-output transformations of individual pyramidal cell dendrites. But despite the importance of subcellular synaptic targeting, virtually nothing is known about whether distinct interneurons selectively target dendrites at a scale finer than domains, i.e., at the level of individual dendritic branches or at specific sub-branch sites. As a result, our understanding of how circuit computations emerge from their individual cellular components in area CA1 remains coarse.

Here we used large-volume array tomography (AT) (Micheva and Smith, 2007; Rah et al., 2013) and transmission electron microscopy (TEM) to examine the organization of synaptic connectivity between molecularly defined interneurons and pyramidal cell dendrites in hippocampal area CA1. The advantages of AT for mapping synaptic connectivity include a 5-fold increase in z axis resolution compared to conventional laser scanning microscopy, sample compatibility with both light and electron microscopy, and relatively rapid imaging of volumes large enough to reconstruct large dendritic trees in their entirety. Exploiting these
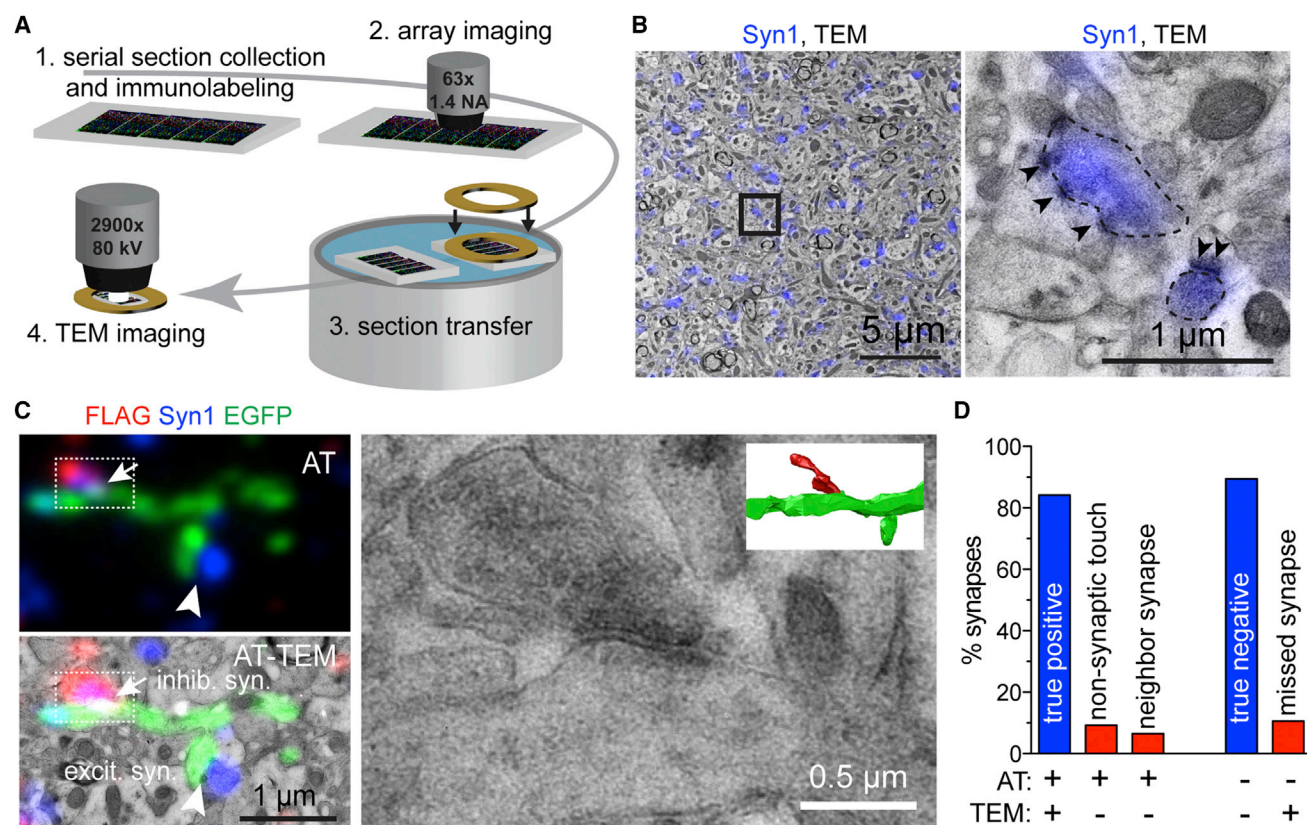
Figure 1. AT Reliably Identifies Synaptic Connectivity between Genetically Labeled Neurons in Mouse CA1

(A) Cartoon of the correlative AT-TEM workflow.

(B) AT-TEM images of Syn1 immunoreactivity from a single section (left) and a magnified view (right) with postsynaptic densities labeled by arrowheads and presynaptic boutons outlined with dashed lines.

(C) AT (top left), AT-TEM (bottom left), and TEM (right) images of an inhibitory synapse between labeled neurons (right inset: synaptic contact reconstructed through serial TEM sections).

(D) Quantification of the accuracy of inhibitory synapse identification between AT and TEM. See also Figure S1 and Movie S1.

advantages, we show that molecularly defined interneurons can target pyramidal cell dendrites in a highly structured fashion, differentially influencing the excitability of the dendritic arbor. Collectively, these results suggest that the cell-type-specific spatial architecture of inhibitory connectivity promotes specific forms of dendritic computation.

RESULTS

AT Reliably Identifies Synaptic Contacts between Labeled Neurons

AT improves upon the z resolution of one- or two-photon microscopy by physically sectioning resin-embedded tissue, which enables light-level synapse identification to be validated directly by performing correlative light and electron microscopy on the same serial ultrathin sections (Collman et al., 2015). We implemented this approach by combining AT and TEM (AT-TEM) (Figure 1A) and screened several antibodies to determine the efficiency and specificity of synaptic labeling. Immunoreactivity from a polyclonal antiserum made against Synaptophysin 1 (Syn1) was present in virtually all CA1 synapses examined across

serial sections (~98%) but was largely restricted to axons (93%) with minimal labeling of postsynaptic structures (0.3%) or mitochondria (0.7%) (Figures 1B, S1A, and S1B; Movie S1, available online). Syn1 puncta size correlated with presynaptic terminal size measured from TEM micrographs (Figure S1C), and puncta were frequently present in synaptic axonal varicosities but rarely in thin-diameter, interbouton stretches of AT-reconstructed interneuron axons (Figure S1D).

To determine directly whether AT can reliably identify inhibitory synapses between interneuron axons and CA1 pyramidal cell dendrites, we imaged ~1 × 10^6 μm^3 of mouse CA1 by AT-TEM. Our sample preparation quenched native fluorescence, so interneurons were infected with Cre-dependent recombinant adeno-associated viral constructs that expressed multiple FLAG epitopes (Viswanathan et al., 2015) and subsequently visualized by immunolabeling FLAG (see Figure S1D). Similarly, pyramidal cells and synapses were visualized by immunolabeling EGFP and Syn1, respectively (Figure 1C). Approximately 84% (64/76) of putative inhibitory synaptic contacts (i.e., those triple labeled for EGFP/FLAG/Syn1 across serial sections) were subsequently identified as synapses in

TEM, while 9% were found to be nonsynaptic touches, and 6% were axons making synaptic contacts onto neighboring processes (Figure 1D). In addition, 89% (34/38) of instances where FLAG axonal signal apposed EGFP dendritic signal but did not exhibit Syn1 were correctly identified as nonsynaptic contacts by TEM, while the other ~11% were synaptic contacts by TEM that were incorrectly assigned as nonsynaptic contacts from the array images (Figure 1D). These data compare favorably with previous reports using similar light-electron microscopy correlative methodologies for excitatory synapse mapping in neocortical circuits (Rah et al., 2013; Schoonover et al., 2014). Lastly, we found that the volumes of dendritic spines obtained separately by AT and TEM serial-section spine reconstructions were well correlated (Figures S1E and S1F). Together, these data demonstrate AT can reliably provide accurate data on synaptic connectivity and morphology.

Division of the Pyramidal Cell Dendritic Tree into Domains and Branch Types

For analysis of large-scale arrays, pyramidal cell arbors were divided into four dendritic domains: apical tuft, distal apical oblique, proximal apical oblique, and basal dendrites. Within these domains, dendrites were further divided into distinct branch types based on branching order: primary, intermediate, and terminal dendrites (Figure 2A). In the distal and proximal apical oblique domains, as well as the apical tuft, the primary dendrites are defined as the main apical trunk with daughter branches divided into intermediate and terminal branches. Because intermediate branches represented a small fraction (<7%) of the obliques, they were not included in our analysis. Basal primary dendrites emerge directly from the soma.

This classification is functionally relevant because primary dendrites have relatively low input impedance, owing to their large size (apical trunk) or their proximity to the soma (primary basals), while terminal dendrites have higher input impedance, owing to their smaller diameter and sealed end (see computational modeling, below). The division of distal and proximal apical oblique branches into two distinct branch types depending on the distance of each branch origin from the soma is in keeping with previous physiological (Andrasfalvy and Magee, 2001; Losonczy et al., 2008) and anatomical (Nicholson et al., 2006) studies suggesting distance-dependent properties of apical oblique branches.

Analyzing the dendritic tree in this way allowed us to ask several important questions about inhibitory connectivity in CA1 (Figure 2B): First, do different types of interneurons target different dendritic domains and branch types? Second, is connectivity to individual dendrites within each branch type random, or do some branches receive more input than others? Lastly, do different interneurons selectively target dendritic branches at precise sub-branch locations, such as the origin or the end of the branches? While the first question has been addressed previously using conventional forms of light microscopy, the remaining questions require the higher resolution afforded by AT. Our strategy was to utilize large-volume AT to map synaptic connections from molecularly defined subsets of interneurons from Cre driver lines (Figures S2A–S2D) onto the dendrites of Thy1-EGFP pyramidal cells, which were primarily located in the deeper portion of the CA1 pyramidal cell layer (Figures S2E and S2F).

Branch-Type Patterns of Inhibitory Connectivity

We first examined the overall distribution of excitatory and inhibitory synapses onto pyramidal cell dendrites using the *VGAT-ires-Cre* mouse (Figure 2C), which expresses *Cre* in the vast majority of GABAergic interneurons (92% of *Gad2-* and 82% of *Gad1*-expressing neurons) (Figure S2A). VGAT^{Cre} synaptic connectivity was highly nonuniform on reconstructed branches from across the pyramidal cell dendritic tree (Figure 2D) and was inversely correlated with the density of dendritic spines (Figures S3A–S3C). These domain-specific patterns of synaptic connectivity are in close agreement with those determined using TEM in CA1 of the rat (Megías et al., 2001), further validating our AT approach.
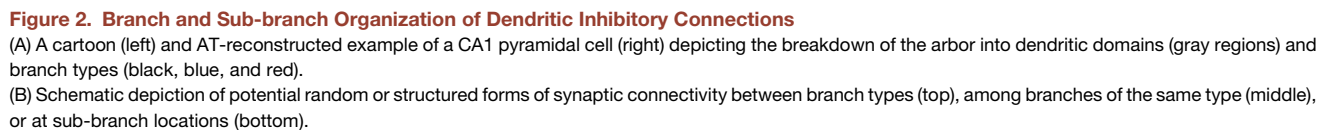
We next sought to determine if inhibitory synaptic connectivity varied systematically between distinct branch types within each domain and, further, whether inhibitory synapses were randomly distributed onto individual branches within each branch type. In the tuft domain, the density of inhibitory synapses did not differ between intermediate (n = 9) and terminal branches (n = 12), despite the large difference between the diameters of these branch types (Figures S3D and S3E). Furthermore, the number of synapses on reconstructed branches within each tuft branch type was found to be consistent with that of a random distribution (Figure S3F).

In the apical oblique domain, the density of inhibitory synapses on the primary apical dendrite (trunk) decreased significantly between the proximal and distal portions (Figures 2D and S3G), similar to previously reported findings in rats (Megías et al., 2001). Inhibitory synapse density did not differ between terminal apical oblique branches in the proximal versus distal domains (Figures S3H and S3I), and nearly all branches within each type (16 of 17 proximal; 17 of 17 distal) had inhibitory synapse numbers consistent with those of a random distribution (Figure S3J).

In the basal domain, a large decrease in the density of inhibitory synapses with increasing branch order was evident (Figures 2D and S3K), which is also consistent with previously reported results in rats (Megías et al., 2001). Across reconstructed terminal basal branches (n = 14), the distributions of inhibitory synapses were found to be consistent with a random distribution (Figure S3L). Collectively, these results demonstrate that the distribution of VGAT^{Cre} inhibitory synaptic contacts can differ among the distinct dendritic branch types present within each domain but that they are randomly distributed across individual branches within each branch type.

Sub-branch Precision of Inhibitory Connectivity

The precise location of inhibitory synaptic connectivity at the sub-branch level has been shown to be important to the integration of excitatory input (Gidon and Segev, 2012) and the plasticity of excitatory synapses (Bar-Ilan et al., 2012). To examine this form of synapse organization, we broke each branch into three compartments by length (near branch origin, 0%–30%; near

Figure 2. Branch and Sub-branch Organization of Dendritic Inhibitory Connections

(A) A cartoon (left) and AT-reconstructed example of a CA1 pyramidal cell (right) depicting the breakdown of the arbor into dendritic domains (gray regions) and branch types (black, blue, and red).

(B) Schematic depiction of potential random or structured forms of synaptic connectivity between branch types (top), among branches of the same type (middle), or at sub-branch locations (bottom).
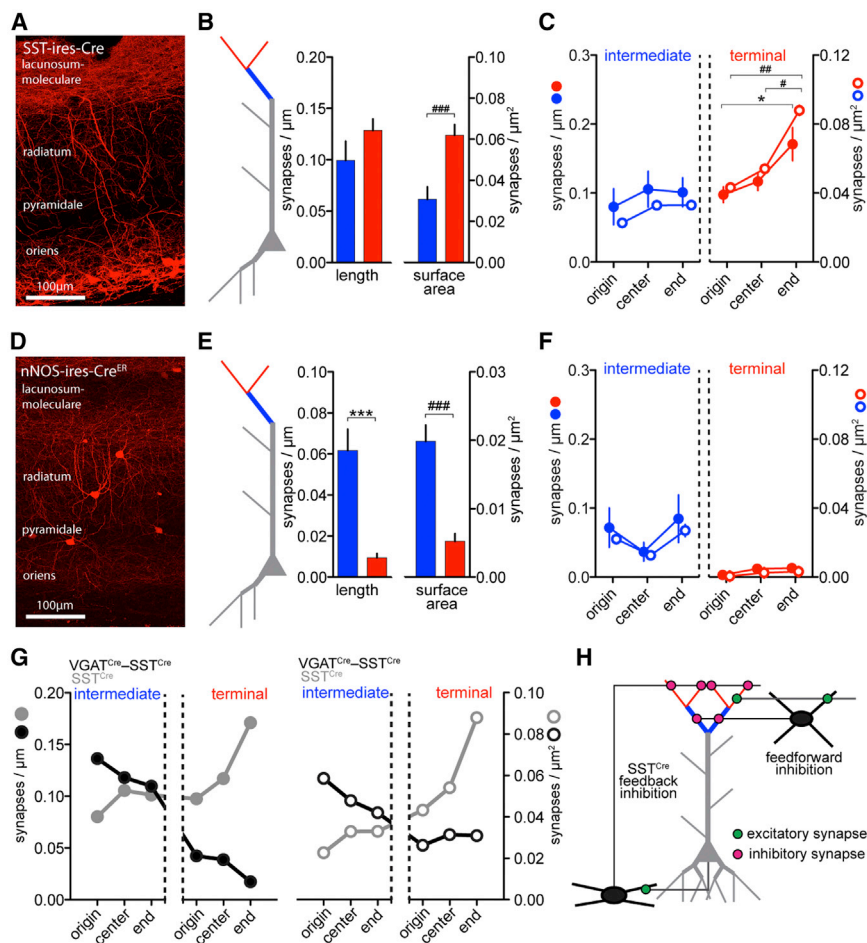
(legend continued on next page)

Figure 3. Synaptic Organization of Tuft Inhibitory Circuits

(A) A portion of the SST^{Cre} array, with FLAG-expressing interneurons in red.

(B) SST^{Cre} synapse density on intermediate and terminal tuft branches as a function of branch length (left) and surface area (right).

(C) SST^{Cre} synapse density at sub-branch locations on intermediate branches and terminal tuft branches as a function of branch length (filled symbols) and surface area (open symbols).

(D) A portion from the nNOS^{CreER} array, with nNOS^{CreER} neurons shown in red.

(E and F) Same as in (B) and (C), respectively, for nNOS^{CreER} synaptic connectivity.

(G) Targeting of putative feedforward inhibitory synapses (VGAT^{Cre} − SST^{Cre}, shown in black) and putative feedback inhibitory synapses (SST^{Cre}, shown in gray) to tuft dendrites as a function of branch length (left) and surface area (right).

(H) Schematic depiction of differential connectivity between feedforward or feedback tuft inhibitory circuits onto tuft branch types.

For (A)–(F), $*p < 0.05$ and $***p < 0.001$ for datasets by dendritic length; $\#p < 0.05$, $\#\#p < 0.005$, and $\#\#\#p < 0.001$ for datasets by dendritic surface area.

All data are presented as mean ± SEM. See also Figures S2–S4 and Movie S2.

branches. Likewise, the density of inhibitory synapses on terminal basal branches decreased by ~50% from the branch origin compared to branch center and near the branch end (Figure 2E). Taken together, these data show that the local inhibitory network targets specific branch types precisely, revealing a gradual transition from inhibition that is biased toward the origin of proximal branches to inhibition biased toward the end of terminal tuft branches.

branch center, 30%–70%; near branch end, 70%–100%; see Figure S3C). Because dendritic diameters taper toward the branch end, data are presented as a function of branch length and branch surface area.

On apical tuft branches, the density of inhibitory synapses did not vary significantly as a function of length along either intermediate or terminal branches. After normalizing for branch surface area, however, a significant increase in synapse density was apparent near the end of terminal branches (Figure 2E), suggesting that a uniform number of synapses along the length of the dendrites may result in a functionally stronger effect near the ends of the terminal branches owing to the low surface area and high input impedance of these branches. In the apical oblique domain, synapse density was similar at sub-branch locations on distal terminal oblique branches but decreased from the branch origin to the branch end in proximal oblique terminal

Recurrent Feedback Inhibition Preferentially Targets the Branch Ends of Terminal Tuft Dendrites

Oriens lacunosum-moleculare (OLM) cells receive excitatory input from CA1, but not CA3 or entorhinal cortex, pyramidal neurons and in turn send a dense axonal projection to CA1 pyramidal cell tuft dendrites to form a local recurrent negative feedback circuit. The vast majority of OLM cells selectively express somatostatin (SST), so the *SST-ires-Cre* driver line (Figures 3A, S2C, and S2D) enables genetic access to these neurons. To examine connectivity between SST^{Cre} axons and apical tuft dendrites, we reconstructed 26 complete tuft

(C) A portion of the VGAT^{Cre} array, with FLAG-expressing interneurons (red) and Thy1-EGFP-expressing CA1 pyramidal cells (green).

(D) The density of both inhibitory (magenta) and excitatory (green) synapses across various dendritic branch types of the pyramidal cell (data shown as mean ± SD; left, by dendritic length; right, by dendritic surface area).

(E) The spatial patterning of VGAT^{Cre} inhibitory synapses at sub-branch locations across different branch types as a function of branch length (filled synapses, left) and branch surface area (open symbols, right). For all plots, $*p < 0.05$, $**p < 0.005$, and $***p < 0.001$ for datasets by dendritic length; $\#p < 0.05$, $\#\#p < 0.005$, and $\#\#\#p < 0.001$ for datasets by dendritic surface area. Scale bar represents 5 μm.

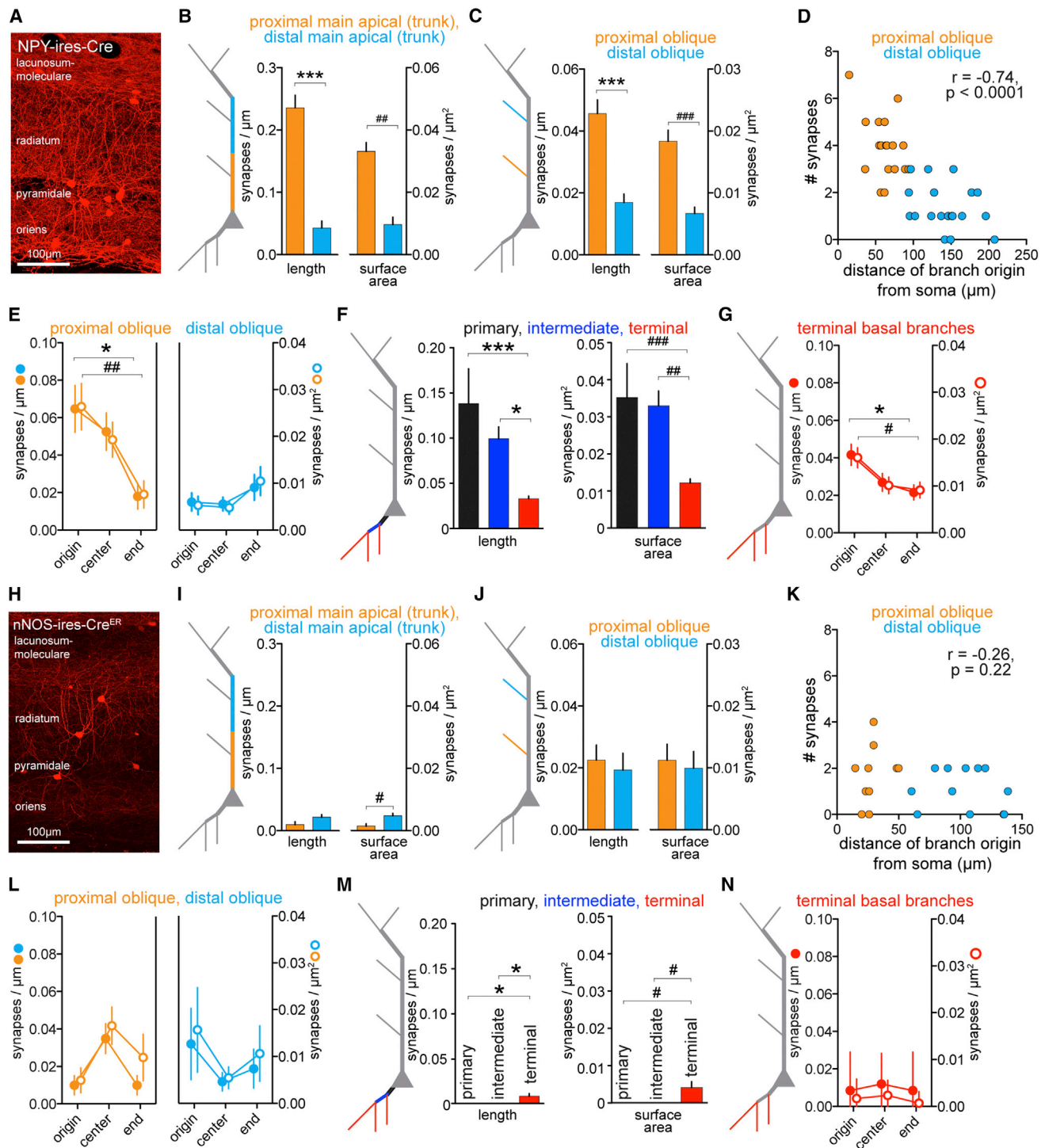All data are presented as mean ± SEM unless otherwise noted. See also Figures S2 and S3.

Figure 4. Synaptic Organization of SR and SO Inhibitory Circuits

(A) A portion of the NPY[Cre] array, with FLAG-expressing interneurons shown in red.

(B) NPY[Cre] synapse density on proximal and distal portions of the proximal main apical (trunk) as a function of branch length (left) and surface area (right).

(C) Same as in (B) but for proximal and distal terminal apical oblique branches.

(D) Relationship between NPY[Cre] synapse number and the distance of the oblique branch origin from the soma.

(E) NPY[Cre] connectivity at the sub-branch level on proximal and distal terminal oblique branches.

(F) The density of NPY[Cre] synapses on basal branch types as a function of branch length (left) and surface area (right).

(legend continued on next page)

branches (n = 11 intermediate and n = 15 terminal branches). When SST^{Cre} synaptic densities were analyzed between branch types as a function of length, we found no significant difference between the number of synapses on intermediate versus terminal branches (Figure 3B). However, after normalizing for the large difference between dendritic surface areas of these two branch types (Figure S4A), terminal tuft dendrites had twice the density of SST^{Cre} synapses compared to the intermediate tuft branches (Figures 3B and S4B). Within each tuft branch type, we found that 4 of 11 intermediate and 2 of 15 terminal branches had SST^{Cre} synapse numbers that differed significantly from a random distribution (Figures S4C and S4D), indicating that there is no strong preference for these synapses to form on particular intermediate or terminal branches within the tuft. Similar to previous reports (Katona et al., 1999), we found that ~30% of SST^{Cre} synaptic contacts formed synapses onto dendritic spines, and the fraction of SST^{Cre}-targeted spines was significantly higher on terminal tuft branches compared to intermediate branches (Figure S4E).

The higher density of synaptic connectivity between SST^{Cre} interneurons and terminal tuft branches is interesting as the presence of the sealed-end boundary renders distal inhibitory synapses more powerful in controlling nonlinear dendritic excitability than proximal synapses (Gidon and Segev, 2012). In further support of differential synaptic targeting between tuft branch types, we found that the density of SST^{Cre} synapses did not differ at the sub-branch level on intermediate branches but increased ~2-fold near the end of terminal branches (Figure 3C). We found no correlation between the distance within stratum lacunosum-moleculare (SLM) (i.e., the distance from the border between stratum radiatum [SR] and SLM) and the density of SST^{Cre} synapses near the branch end (data not shown), suggesting that these results could not be explained by a simple increasing gradient of SST^{Cre} axonal connectivity within SLM. These results suggest that SST^{Cre}-mediated feedback inhibition may be functionally more potent toward the end of terminal branches.

Tuft Feedforward Inhibitory Circuits Preferentially Target Intermediate Tuft Dendrites

Interneurons that provide feedforward inhibition to the tuft include neurogliaform cells (NGFCs), perforant path-associated cells, and other unclassified interneuron types that receive excitatory inputs from CA3 and/or entorhinal cortex neurons (Klausberger, 2009). Synapses from perforant path-associated cells onto tuft dendrites are estimated to be sparse (~12 per pyramidal neuron in the rat; Bezaire and Soltesz, 2013), so we focused on the more prevalent NGFCs and their synaptic connectivity to tuft dendrites.

NGFCs commonly express neuropeptide Y (NPY) and neuronal nitric oxide synthase (nNOS) (Price et al., 2005) and can be visualized in both *NPY-ires-Cre* and *nNOS-ires-CreER* driver lines (Figure S2D). In the NPY^{Cre} line, however, *Cre* is expressed in ~50% of SST+ neurons (Figure S2C), confounding the ability to separate the NPY^{Cre} NGFC synapses from those of NPY^{Cre} OLM cells on tuft branches. *Cre*-expressing neurons in the *nNOS-ires-CreER* line, however, rarely coexpress *SST* (~3%; Figure S2C) and thus allow selective genetic access to nNOS+ NGFCs (Figure 3D).

The organization of nNOS^{CreER} synapses on tuft branch types was largely reciprocal to that of SST^{Cre} synapses. Despite their low density, nNOS^{CreER} synapses showed a marked connectivity preference for intermediate branches compared to terminal branches (n = 7 and 10 branches, respectively) (Figures 3E, S4F, and S4G). Within each branch type, none of the reconstructed tuft branches differed significantly from the variability expected from a random distribution (Figures S4H and S4I). In further contrast to the organization of SST^{Cre} synapses, we found no differences in the density of nNOS^{CreER} synapses at the sub-branch level (Figure 3F), and nNOS^{CreER} synapses targeting dendritic spines were rare (Figure S4J).

The interneurons labeled in the nNOS^{CreER} line comprise only a small fraction of the total synaptic connectivity from feedforward inhibitory circuits onto tuft branches. It is possible, however, to compare the overall density and organization of feedforward inhibitory synapses by subtracting the density of SST^{Cre} inhibitory synapses from that obtained from the VGAT^{Cre} dataset (i.e., VGAT^{Cre} − SST^{Cre}). Based on this analysis, we estimate that inhibitory synapses from SST^{Cre} interneurons account for ~40% of the synapses to intermediate tuft branches, but more than 70% of those on the terminal tuft branches (Figure 3G). Thus, we conclude that synapses belonging to feedforward and feedback inhibitory circuits preferentially target tuft intermediate and terminal dendrites in a reciprocal fashion (Figure 3H).

NPY^{Cre} Interneurons Preferentially Target the Origin of Terminal Branches in Proximal Apical Oblique and Basal Dendrites

The Schaffer collaterals (CA3 axons) provide the major afferent excitatory pathway onto the apical oblique and basal dendrites of CA1 pyramidal cells. Several GABAergic cell types target these dendrites, including bistratified cells, ivy cells, basket cells, apical dendrite innervating cells, and Schaffer collateral-associated cells (Klausberger, 2009). In contrast to tuft inhibitory circuits, many of these interneurons receive both CA3 and CA1 input and thus can act as both feedforward and feedback circuit elements (Buhl et al., 1996; Halasy et al., 1996; Klausberger et al., 2004).

The NPY^{Cre} mouse driver line enables genetic access to a large subset of interneurons targeting pyramidal cell dendrites in stratum oriens (SO) and SR (Figure 4A). In area CA1 of the rat, NPY is expressed in both bistratified (Klausberger et al., 2004) and ivy cells (Fuentealba et al., 2008), and in situ hybridization confirmed that some *Cre*-expressing neurons in the

---

(G) The density of NPY^{Cre} synapses at the sub-branch level of terminal basal branches.

(H–N) Same as in (A)–(G), respectively, depicting the distribution of nNOS^{CreER} synapses.

For all plots, *p < 0.05 and ***p < 0.001 for datasets by dendritic length; #p < 0.05, ##p < 0.005, and ###p < 0.001 for datasets by dendritic surface area. All data are presented as mean ± SEM. See also Figures S2 and S5.

NPY[Cre] driver line coexpressed markers of both cell types (data for bistratified cells are as follows: *Parvalbumin* [*PV*], 8%; *SST*, 29%; data for ivy cells are as follows: *nNOS*, 25%) (Figure S2C).

NPY[Cre] synapses were found to account for ~75% of the VGAT[Cre] inhibitory synapse density on proximal and distal portions of the primary apical (trunk) dendrite in SR (Figure 4B). However, the density of NPY[Cre] synapses consistently differed between terminal branches from proximal and distal apical oblique dendrites (80% and 35% of the VGAT[Cre] density, respectively; n = 18 and 19), with proximal branches exhibiting a 3-fold higher density of inputs than distal ones (Figure 4C). Synapse number (Figure 4D) and density (Figure S5A) correlated inversely with the distance of branch origin from the soma. No evidence for structured forms of NPY[Cre] synaptic connectivity was found between individual terminal oblique branches, as branches from within each domain were found to be within the expected variability of a random distribution (Figure S5B). In further support for branch-specific targeting, NPY[Cre] synapses on proximal, but not distal, branches systematically formed synaptic contacts near the branch origin and largely avoided the branch end (Figure 4E).

Across all basal branches, NPY[Cre] synapses account for ~40%–50% of the VGAT[Cre] inhibitory synapse density, and their density decreased significantly from primary and intermediate branches to terminal basal branches (Figure 4F). Within a large set of reconstructed terminal basal branches (n = 29), we found only a single branch that deviated significantly from a random distribution (Figure S5B). NPY[Cre] synapse density at the sub-branch level revealed an approximate 50% decrease from the branch origin to the branch end on terminal basal branches (Figure 4G). Thus, in the terminal branches of both proximal apical oblique and basal dendrites, NPY[Cre] inputs selectively target the branch origin.

nNOS[CreER] Ivy Cells Synapse onto Apical Oblique and Basal Branch Types without Sub-branch Structure

Since neurons in the NPY[Cre] line that project to apical oblique and basal dendrites include both ivy and bistratified cells, we analyzed the synaptic connectivity from nNOS[CreER] interneurons onto apical oblique and basal dendrites to specifically examine the organization of ivy cell synapses (Figure 4H). nNOS-expressing neurons represent only a fraction of the total hippocampal ivy cell population (Tricoire et al., 2010) but do not include appreciable numbers of other interneuron cell types that target the apical oblique or basal domains (Fuentealba et al., 2008). We detected *Cre* expression in 83% of *nNOS*-expressing cells and confirmed that *Cre*-expressing neurons frequently coexpressed *NPY* (74%) but rarely markers of bistratified cells (e.g., *PV*, 2%; *SST*, 4%) (Figure S2).

Unlike NPY[Cre] synapses, nNOS[CreER] axons rarely formed synaptic contacts with the main apical (trunk) dendrite (Figure 4I). In further contrast to NPY[Cre] interneurons, nNOS[CreER] synaptic connectivity to terminal oblique branches did not differ between proximal and distal branches (Figure 4J) and was not correlated with the location of branch origin (Figures 4K and S5D). The number of nNOS[CreER] synapses on dendritic branches did not differ from a random distribution for nearly all SR dendrites sampled

(11 of 12 distal apical oblique branches; 11 of 11 proximal apical oblique branches) (Figure S5E). In further support of a random pattern of synaptic connectivity, the distribution of nNOS[CreER] inhibitory synapses among dendrites was not found to differ consistently at the sub-branch level on apical oblique branches (Figure 4L).

In the basal dendritic domain, nNOS[CreER] inhibitory synapses were not observed on primary and intermediate branches and remained sparse on terminal basal branches (Figure 4M). Most terminal basal branches (11 of 13) had synapse numbers that fell within the variability expected for a random distribution (Figure S5E). Moreover, no differences were evident in the density of nNOS[CreER] inhibitory synapses at the sub-branch level (Figure 4N). Taken together, our data show that nNOS[CreER] inhibitory synapses are randomly organized on the terminal branches of apical oblique and basal dendrites.

PV[Cre] and SST[Cre] Interneurons Show Weak but Reciprocal Distance-Dependent Gradients of Connectivity to Apical Oblique Dendrites

We analyzed the distribution of inhibitory synapses onto apical oblique and basal dendrites from PV[Cre] or SST[Cre] driver lines (Figure S5). Cre expression in these neurons enables genetic access to a subset of dendrite-targeting bistratified cells (Royer et al., 2012) (Figure S2). In addition, Cre-expressing neurons in the PV[Cre] line include basket cells that frequently form synapses onto the proximal apical oblique and basal dendrites and axo-axonic cells that target the pyramidal cell axon (Halasy et al., 1996), while Cre-expressing neurons in the SST[Cre] driver line include tuft-targeting OLM cells.

In terminal branches of proximal and distal apical oblique domains, we found that synaptic connections from either PV[Cre] or SST[Cre] interneurons were sparse (Figure S5). Interestingly, the number and density of PV[Cre] synapses were found to significantly correlate inversely with the distance of branch origin from the soma (Figure S5H), while the number and density of synapses from SST[Cre] cells showed a nonsignificant trend toward a positive correlation (Figure S5K). In the basal domain, PV[Cre] synapses showed strong selectivity for primary branches (Figure S5I) and could account for more than 50% of the VGAT[Cre] synapse density. In contrast, SST[Cre] axons avoided both primary and intermediate basal branches entirely, with very small numbers of synapses on the terminal basal dendrites (Figure S5L).

The Number of Inhibitory Synapses on Pyramidal Cell Dendrites

To put our density measurements in context with the dendritic morphology of CA1 pyramidal cells, we reconstructed complete dendritic domains from pyramidal cells and used these to estimate the number of axospinous excitatory synapses and inhibitory synapses from local interneurons (Figure 5A). Projecting our branch-level findings onto AT-reconstructed apical tuft domains (n = 3) resulted in an estimate of 1,301 ± 41 dendritic spines (677 ± 60 on terminal tuft branches and 623 ± 99 on intermediate tuft branches) and 288 ± 38 VGAT[Cre] inhibitory synapses (154 ± 13 on terminal tuft branches and 134 ± 44 on intermediate tuft branches) spread across a
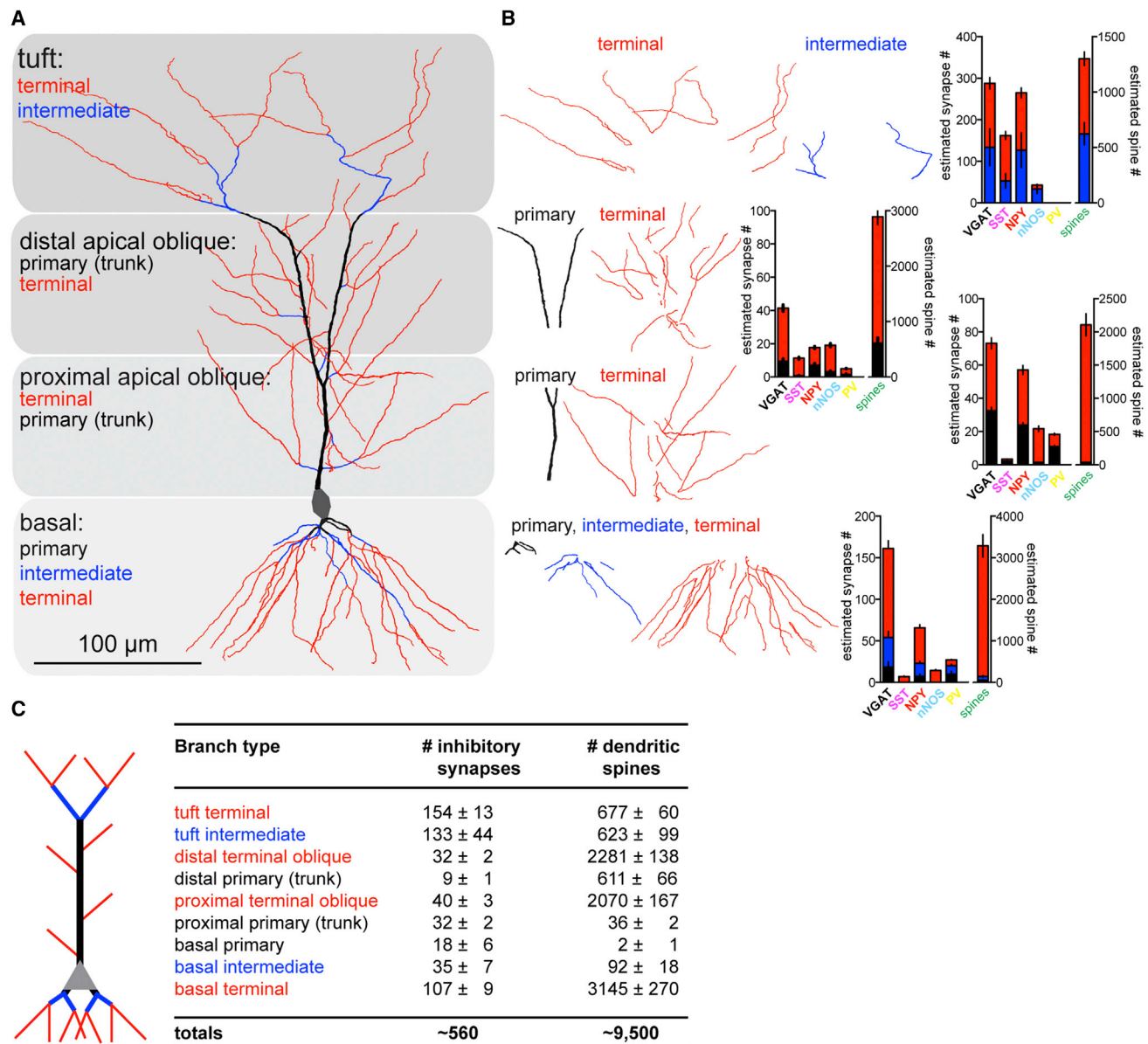
A

tuft:
terminal
intermediate

distal apical oblique:
primary (trunk)
terminal

proximal apical oblique:
terminal
primary (trunk)

basal:
primary
intermediate
terminal

100 μm

B

terminal   intermediate

primary   terminal

primary   terminal

primary, intermediate, terminal

C

Branch type	# inhibitory synapses	# dendritic spines
tuft terminal	154 ± 13	677 ± 60
tuft intermediate	133 ± 44	623 ± 99
distal terminal oblique	32 ± 2	2281 ± 138
distal primary (trunk)	9 ± 1	611 ± 66
proximal terminal oblique	40 ± 3	2070 ± 167
proximal primary (trunk)	32 ± 2	36 ± 2
basal primary	18 ± 6	2 ± 1
basal intermediate	35 ± 7	92 ± 18
basal terminal	107 ± 9	3145 ± 270
totals	**~560**	**~9,500**

Figure 5. Estimate of Synapse Numbers across Domains and Branch Types of CA1 Pyramidal Cells
(A) Deconstruction of a representative CA1 pyramidal cell into its domains and branch types.
(B) The estimated number of synapses from each interneuron subset across each dendritic domain and branch type (tuft, n = 3; apical oblique, n = 5; basal, n = 4), as well as the estimated number of dendritic spines.
(C) Estimate of the total number of local VGAT[Cre] inhibitory synapses, as well as the number of dendritic spines as a function of branch type.
All data are presented as mean ± SEM.

typical apical tuft (Figures 5B and 5C). SST[Cre] synapses could account for slightly more than half of all inhibitory synapses (~55%, 162 ± 25) and more than two-thirds of those on terminal tuft branches (~71%, 109 ± 9). NPY[Cre] tuft-targeting interneurons could account for most tuft synapses (~90%, 264 ± 36). In contrast, nNOS[CreER] synapses could account for only a small fraction of synapses within the apical tuft (~15%, 42 ± 10), with most of these targeting intermediate branches (33 ± 11). The remaining inhibitory synapses on terminal and

intermediate tuft branches (~30 and ~50, respectively) likely represent inputs from nNOS− NGFCs and perforant path-associated cells.

We reconstructed several apical oblique domains (n = 5, three domains with a single main apical trunk and two with a bifurcating trunk morphology) and examined synapse numbers across the distal and proximal branches. In the distal oblique domain, we estimate there are 2,892 ± 140 dendritic spines but only 41 ± 2 VGAT[Cre] inhibitory synapses, which largely reflects the low

density of inhibitory connections on the distal portion of both the main apical and distal terminal oblique branches (Figures 5B and 5C). The majority of inhibitory synapses within this domain are found on the terminal oblique branches (distal main apical, 9 ± 1; distal terminal obliques, 32 ± 2). On these branches, nNOS[CreER] synapses represent the largest portion of terminal oblique synapses (~50%, 16 ± 1), presumably reflecting nNOS+ ivy cell inputs to these branches. The large fraction of remaining oblique inhibitory synapses that are unaccounted for likely comes from Cholecystokinin (CCK)-expressing interneurons.

In the proximal apical oblique dendritic domain we estimate there are ~2,106 ± 168 dendritic spines and 73 ± 5 VGAT[Cre] inhibitory synapses (Figures 5B and 5C). The near-2-fold difference in inhibitory synapse numbers between the proximal and distal apical oblique domains is due to the relatively high density of connections made onto the proximal portion of the main apical (trunk). However, the total number of synapses on the terminal oblique branches remained slightly higher compared to those contacting the main apical (terminal obliques, 41 ± 2; main apical, 32 ± 2). We found that NPY[Cre] synapses represent a similarly large fraction of the inputs onto both the proximal main apical and the proximal terminal oblique branches (~75% for both), presumably reflecting combined inputs from NPY+ ivy cells and NPY+ bistratified cells. Synapses from PV[Cre] neurons contributed ~50% to the connections found on the main apical (trunk).

Across reconstructed basal domains (n = 4), we estimate there are ~3,239 ± 259 dendritic spines and 161 ± 8 VGAT[Cre] inhibitory synapses (Figures 5B and 5C). Despite the high density of inhibitory connections onto the primary or intermediate branches, their connections comprise a relatively small number due to their small size and number of branches, so the majority of inhibitory synapses contact the terminal branches (~66%, 107 ± 9). Similar to the proximal oblique domain, NPY[Cre] synapses were found to comprise the largest fraction (40%–50%) of the total input number across these branches. Across all dendritic domains, our findings suggest there are ~9,500 dendritic spines and ~560 dendritic inhibitory synapses from local interneurons on a mouse CA1 pyramidal cell (Figure 5C).

Simulations to Assess the Functional Implications of Precisely Targeted Dendritic Inhibition

How do these synaptic distributions influence the integration of excitatory inputs? We constructed a computational model using two AT-reconstructed CA1 pyramidal cell morphologies (Figure S6) with passive and active properties similar to those used previously (Katz et al., 2009), which reproduced experimental data on backpropagating action potentials (bAPs) and dendritically initiated spikes (see Supplemental Experimental Procedures). Excitatory and inhibitory synapses were distributed across the dendrites such that their densities conformed to the experimental results.

We performed simulation experiments that were structured to allow comparison among three conditions: excitation alone, excitation with one type of inhibition (e.g., SST+ inhibition in the apical tuft), and excitation with a complementary form of inhibition (e.g., SST− inhibition in the apical tuft). Each set of simulations consisted of a trial from each condition, with excitatory synapses initially as-

signed in a stochastic manner and then held constant across the set. Inhibitory synapses were assigned stochastically from the experimentally observed distributions for the two trials from each set with inhibition, and each experiment comprised 100 sets of simulations. In order to isolate how the spatial organization of inhibitory synapses influenced dendritic integration, all dendritic inhibitory synapses were assumed to have identical conductances and kinetics, which were taken from a previous report using pyramidal cell-interneuron paired recordings (Maccaferri et al., 2000).

Simulation of Synaptic Input to the Apical Tuft Dendrites

We first simulated the integration of perforant path-like input to tuft dendrites by activating excitatory synapses either alone (n = 100 synapses) or coincident with SST+ or SST− inhibition (n = 20 synapses) and examined the voltages at two tuft locations (one terminal and one intermediate branch) and at the soma (Figure 6A). In simulations where excitatory synapses were activated in the absence of inhibition, dendritic spikes (voltage deflections >25 mV) were first initiated in the high-impedance terminal branches in virtually all trials (98/100), and they attenuated as they propagated from the tuft toward the soma. Consistent with previous work (Jarsky et al., 2005), activation of tuft excitatory synapses did not induce somatic action potentials (APs), even in the absence of inhibition.

Of the 98 simulations in which excitation alone elicited a dendritic spike in the terminal tuft branch, either SST+ or SST− forms of inhibition blocked dendritic spikes in most sets (58/98); in a few sets (5/98), neither blocked dendritic spikes. Of the remaining 35 sets, activation of SST+ synapses was more than twice as likely to block tuft spikes (25/35) than was activation of SST− inhibitory synapses (10/35) (Figure 6B). When comparing the difference in mean voltage profiles for these simulations, it was evident that the SST+ and SST− synaptic distributions differentially hyperpolarized tuft dendrites in a branch-type-dependent manner, as expected from their synaptic distributions: SST+ inhibition selectively hyperpolarized the terminal branches, while SST− inhibition selectively hyperpolarized the intermediate tuft branches (Figure 6C). Results were qualitatively similar over a large range of inhibitory synapse numbers or conductances as well as in simulations using a second CA1 pyramidal cell morphology (Figures S6A and S6B).

Do SST+ inhibitory synapses block terminal tuft branch spikes more efficiently due to their selective branch-level targeting, or does their sub-branch location contribute to this effect? To address this question, we performed two additional sets of simulations: first, we swapped the SST+ synapse density between intermediate and terminal tuft branches (SST+[swapped]), and second, we reversed the spatial gradient of SST+ synapses (SST+[reversed]) on terminal tuft branches such that these synapses preferentially contacted the branch origin. While the SST+[swapped] condition increased the incidence of trials with tuft spikes by ~50%, we found that the SST+[reversed] condition had little effect on tuft spiking (Figure S6C). As we could replicate the stronger efficacy of inhibitory synapses placed near the branch end compared to those placed near the branch origin on dendritic spiking in our model (Gidon and Segev, 2012) (Figure S6D),
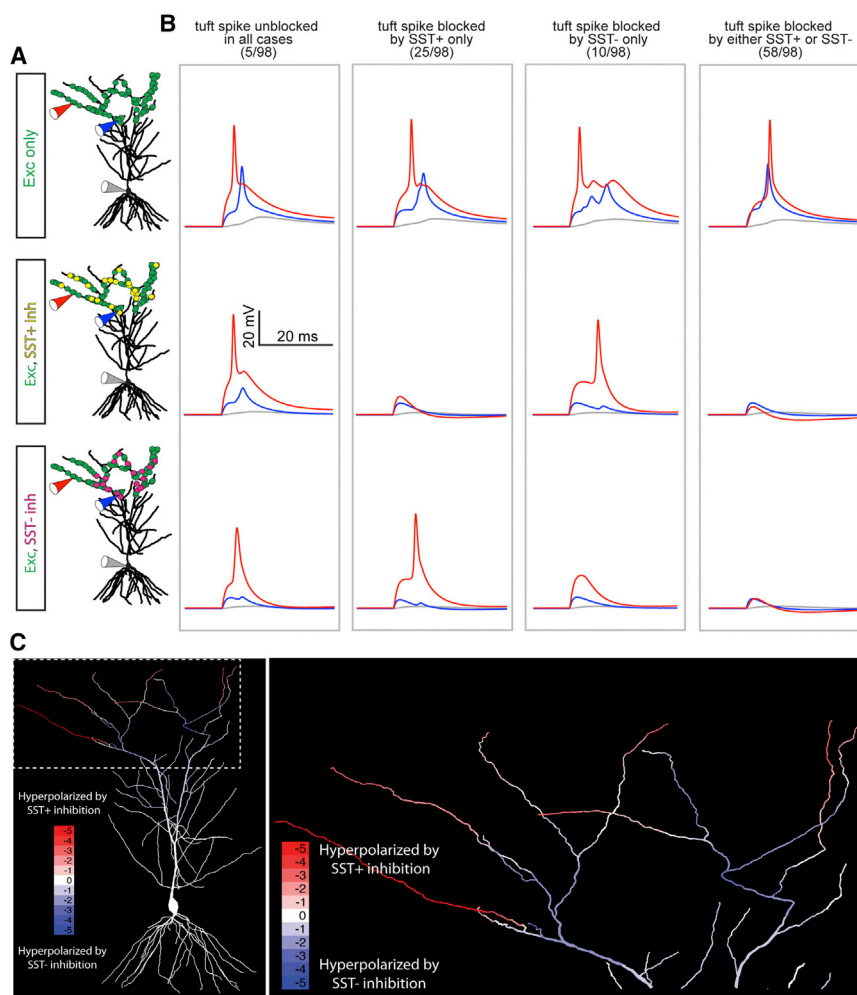
Figure 6. Feedforward and Feedback Inhibitory Circuits Differentially Control Tuft Dendritic Excitability

(A) Representative example of a simulation set with excitatory synapses (top; green, n = 100), SST+ synapses (middle; yellow, n = 20), and SST− synapses (bottom; magenta, n = 20) placed onto the tuft dendritic morphology of a CA1 pyramidal cell. The electrodes depict recording sites in the tuft (red, terminal branch; blue, intermediate branch) and at the soma (gray).

(B) Voltage traces from the simulations, with each column showing results from a simulation set and each row representing the condition. Sets in which the excitation-alone condition did not generate a dendritic tuft spike are not shown (2 of 100 sets).

(C) Mean branch voltage changes as a result of activation of SST+ and SST− inhibitory synapses in tuft dendrites shown across the neuron (left) and zoomed in on the tuft branches (right). See also Figure S6.

14 sets had somatic spikes that were blocked only by activation of NPY+ inhibitory synapses; we never observed a trial in which coactivation of NPY− synapses blocked a somatic spike but NPY+ synapses did not (Figure 7B). These results show that the spatial organization of NPY+ synapses produces more potent prevention of somatic spikes than that of NPY− synapses over a range of excitatory input configurations.

For excitatory input configurations that produced subthreshold somatic responses (the 45 out of 100 above), we found that NPY+ inhibition preferentially hyperpolarized the proximal apical dendrites, whereas NPY− inhibition preferentially hyperpolarized distal apical oblique dendrites (Figure 7C), as expected from their synaptic distributions. Similar spatial patterns of voltage changes were observed when we examined the effect of inhibition on bAPs from simulations where excitation remained suprathreshold despite coactivation of either NPY+ or NPY− inhibition: proximal apical oblique branches were markedly more hyperpolarized by NPY+ inhibition, whereas distal oblique branches were more hyperpolarized by NPY− inhibition.

Do NPY+ inhibitory synapses preferentially block AP initiation due to their selective branch targeting, or does the localization of these synapses toward the origin of these branches contribute to this effect? To distinguish these possibilities, we performed several synaptic-swapping experiments analogous to those from the tuft simulations. In the first iteration, we swapped the density of proximal terminal oblique branches with that of the distal terminal oblique branches (NPY+$_{swapped}$) and found that this reduced the block of APs in NPY+ trials by 34% (Figure S6E). Similarly, reversing the observed gradient of synapse density along proximal oblique branches (NPY+$_{reversed}$) also reduced the ability of NPY+ inhibition to block somatic APs, though the
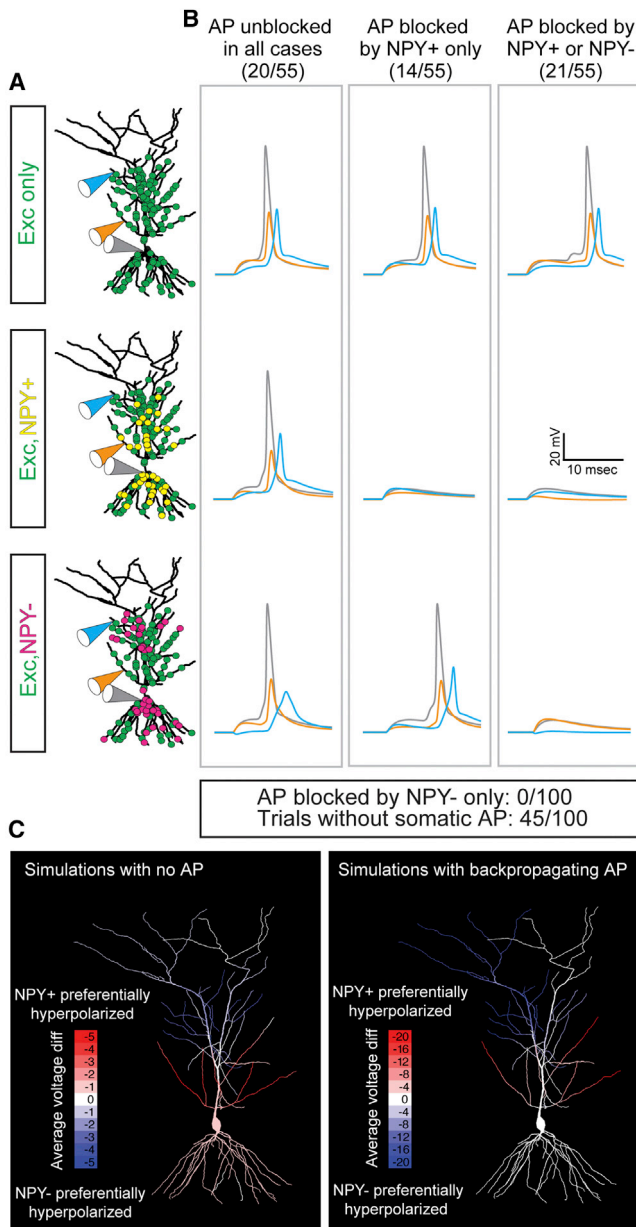
this negative result reflects the difference between a synaptic gradient and synapses placed at these locations in a binary manner, as well as the stochastic selection of inhibitory synapses in the simulation sets. Collectively, these results suggest that the selectivity of SST+ synapses for terminal tuft branches is the predominant factor mediating their control over tuft dendritic spiking, with a smaller contribution from their sub-branch synaptic organization.

Simulation of Synaptic Input to Basal and Apical Oblique Dendrites

Next, we considered Schaffer collateral-like excitation onto the basal and apical oblique dendrites and examined the effect of NPY+ or NPY− inhibitory synapses on dendritic and somatic excitability. Excitatory synapses (n = 140) were activated on branches in both SR and SO simultaneously, either without inhibition or coincident with NPY+ or NPY− inhibition (n = 40 synapses) (Figure 7A). In the 100 excitation-alone trials, somatic APs were initiated in 55 trials. Of these 55 sets of simulations, both the NPY+ and NPY− trials blocked spikes in ∼39% of trials (21/55), while somatic spikes were not blocked by either form of inhibition in ∼36% of trials (20/55). Interestingly, the remaining

A

B

C

AP blocked by NPY- only: 0/100
Trials without somatic AP: 45/100

Figure 7. NPY+ and NPY− Synapses Differentially Control Somatic Spiking and AP Backpropagation

(A) Representative example of a set of simulations with excitatory synapses (top; green, n = 140), NPY+ synapses (middle; yellow, n = 40), and NPY− synapses (bottom; magenta, n = 40) placed onto the apical oblique and basal dendritic morphology of a CA1 pyramidal cell. The electrodes depict recording sites in the oblique branches (blue, distal oblique; orange, proximal oblique) and at the soma (gray).

(B) Voltage traces from the simulations, with each column showing results from a simulation set and each row representing the condition. Simulation results from sets in which the excitation-alone condition did not generate a dendritic somatic spike are not shown (45 of 100 sets); in addition, there were no simulation sets in which a somatic spike was blocked by NPY−, but not NPY+, inhibition.

(C) Mean branch voltage changes by activation of NPY+ and NPY− inhibitory synapses from subthreshold (left) and suprathreshold (right) simulations. Note that the discrepancy of the average voltage difference between the left and

effect size was smaller (~14%; Figure S6E). Collectively, results from both the tuft and oblique simulations show that the branch targeting of SST[Cre] and NPY[Cre] inhibition is a critical factor enabling these interneurons to selectively influence dendritic computations in pyramidal cells.

DISCUSSION

The AT approach utilized here enabled reconstruction of cell-type-specific inhibitory synaptic connectivity onto more than 350 complete dendritic branches, and our results reveal unprecedented precision with which inhibitory cell types target their synapses onto pyramidal cell dendrites. The potential functional roles of these cell-type-specific synaptic architectures were explored through computational modeling, where we found that these distributions differentially influenced dendritic spiking as well as AP initiation and backpropagation. These results are consistent with previous reports from computational models (Gidon and Segev, 2012; Hao et al., 2009; Koch et al., 1983) and in vitro slice experiments (Hao et al., 2009; Jadi et al., 2012; Müllner et al., 2015), demonstrating that branch and sub-branch locations are strong determinants of how inhibitory synapses ultimately contribute to dendritic integration.

The spatial patterning of specific inhibitory connections observed here suggests several ways that interneuron cell types might selectively influence dendritic computation in CA1 pyramidal cells. In the tuft, activation of nNOS+ NGFCs, which preferentially target intermediate branches and spike in temporal alignment with the maximum activity in the perforant path during the CA1 theta-cycle oscillation (Fuentealba et al., 2010), could act as a spatiotemporally focused gate that regulates tuft output through a divisive form of gain control via their on-path synaptic location (i.e., between the excitatory synaptic site and the soma) (Jadi et al., 2012). In contrast, the recruitment of SST+ OLM interneurons marks a dramatic spatial redistribution of tuft inhibition to primarily off-path locations (i.e., outside the path from the excitatory synaptic site to the soma) near the sealed end of terminal tuft dendrites. Such a switch is facilitated by the direct inhibition of feedforward tuft circuits by OLM cells (Elfant et al., 2008). In our tuft simulations, activation of SST+ synapses strongly inhibited dendritic spikes in the terminal branches, providing support for a model in which the local OLM recurrent feedback inhibitory network is optimally positioned to control distal tuft spike initiation rather than spike propagation toward the soma. These findings, as well as the higher proportion of SST+ synapses directly targeting dendritic spines, have implications for synaptic plasticity as tuft dendritic spikes have been linked to long-term potentiation of CA1 tuft synapses in vitro (Golding et al., 2002; Kim et al., 2015).

In the apical oblique dendritic domains, we find that the density of NPY+ synapses decreases as a function of the distance of the oblique branch origin from the soma. These data also imply that NPY− dendritic inhibitory synapses, including those

right main apical trunk branches within each condition is due to the more efficient AP backpropagation in the left trunk branch, similar to what has been previously reported for CA1 pyramidal cells in vitro (Spruston et al., 1995). See also Figure S6.

from CCK-expressing interneurons, are organized onto the apical oblique branches with a reciprocal gradient of connectivity and provide a substantial portion of the inhibitory synapses made onto distal oblique branches. In the case of NPY+ synapses, their selective synaptic targeting both at the branch and sub-branch level contributes to the potent block of AP initiation. Interestingly, activation of only a few excitatory synapses in these proximal oblique branches can initiate strong dendritic Na$^+$ spikes (Losonczy et al., 2008), which appear resistant to the effects of inhibition (Müller et al., 2012). As a result, NPY+ inhibition might act to selectively inhibit weakly excitable proximal branches while allowing highly excitable branches to drive somatic spiking. Moreover, bAPs have been implicated in the plasticity mechanisms underlying the formation of these strong branch spikes (Losonczy et al., 2008), so NPY+ inhibition, through its modulation of bAP amplitudes, might confer branch-selective inhibitory control over the dendritic-somatic-spike-associative signals as well as spike-timing-dependent forms of synaptic plasticity.

Not all interneuron subtypes examined here showed strong evidence for structured connectivity to pyramidal cell dendrites. In particular, the distribution of synapses from nNOS^{CreER} interneurons on apical oblique dendrites was not found to show branch-level selectivity or patterned sub-branch targeting. The lack of spatially structured inputs from nNOS^{CreER} interneurons is consistent with a role for CA1 ivy cells in providing widespread, tonic inhibitory signaling independent of behavioral state (Lapray et al., 2012). It should be noted, however, that neurons expressing nNOS may signal through volume transmission of GABA (Oláh et al., 2009; Szabadics et al., 2007), and these non-synaptic sources of inhibition were missed entirely in the present analysis. Similarly, it is possible that systematic differences in subsynaptic ultrastructure, such as the number of synaptic release sites or other features that our AT approach cannot resolve, could also contribute to differences in how interneuron cell types exert their control over integration in pyramidal cells.

Taken together, our findings show that distinct subsets of dendrite-targeting interneurons exhibit a remarkable, previously unappreciated structure in their organization on pyramidal cell dendrites. Such structure within the local inhibitory network provides further support for the hypothesis that individual branches can act as fundamental units of computation in pyramidal cells (Branco and Häusser, 2010; Jadi et al., 2014). Moreover, recent reports have demonstrated that distinct groups of hippocampal and neocortical interneurons directly respond to task-relevant stimuli (Gentet et al., 2012; Kvitsiani et al., 2013; Lovett-Barron et al., 2014; Pi et al., 2013), implying that spatially structured synaptic targeting in the local inhibitory network could be a critical factor in driving forms of circuit computation that underlie specific behaviors.

EXPERIMENTAL PROCEDURES

Mice
All experiments were conducted in accordance with NIH guidelines and with approval of the Janelia Institutional Animal Care and Use Committee. *VGAT-ires-Cre* (RRID: IMSR_JAX:016962) (Vong et al., 2011), *SST-ires-Cre* (Lovett-Barron et al., 2012), *PV-ires-Cre* (RRID: MGI_3716104) (Hippenmeyer et al., 2005), *nNOS-ires-Cre^{ER}* (RRID: MGI_4947130) (Taniguchi

et al., 2011), and *NPY-ires-Cre* (Milstein et al., 2015) mice were crossed with the Thy1-EGFP line M (RRID: IMSR_JAX:007788, array tomography experiments) or line H (RRID: IMSR_JAX:003782, AT-TEM experiments) (Feng et al., 2000).

Intracranial Viral Injections
Recombinant viral vectors (serotype 2/1) were used to drive Cre-dependent expression of spaghetti monster FLAG tags (Viswanathan et al., 2015) in male adult mice (10–12 weeks of age). Virus was injected as described (Royer et al., 2012). Tamoxifen, dissolved in sunflower oil (Sigma) at 50 mg/ml, was used to drive Cre recombinase activity in the *nNOS-ires-Cre^{ER}* line beginning 2 weeks after viral injection via oral gavage for 5 consecutive days, from 14–19 and 28–33 days after viral injection. See Supplemental Experimental Procedures.

Sample Preparation
Perfusion-fixed coronal mouse slices containing the dorsal CA1 were frozen using a high-pressure freezer (Wohlwend), freeze substituted, infiltrated with Lowicryl HM20 Monostep resin (Electron Microscopy Sciences) at $-45°$C, and polymerized for 48 hr under UV light (405 nm). See Supplemental Experimental Procedures.

Correlative AT-TEM
Coverslips (High Precision) were coated with Pioloform followed by 4–5 nm of carbon. The 70 nm serial sections were processed and imaged using identical immunolabeling protocols to those of large-scale arrays (see below). The Pioloform support film was etched from the coverslip with 1.5% hydrofluoric acid and floated onto double-distilled H$_2$O, and Synaptek TEM grids (Ted Pella) were dropped over the section ribbons. For more detailed instructions, see Watanabe et al. (2014).

Grids were stained with 5% uranyl acetate for 5 min, rinsed in double-distilled H$_2$O, stained with Sato's lead, and imaged at 3.8 × 3.8 nm pixel resolution using a Tecnai Spirit BioTWIN TEM operated at 80 kV using Leginon (Suloway et al., 2005). AT and TEM images were assembled, montaged, and aligned using custom alignment software and transformation algorithms in TrakEM2. See Supplemental Experimental Procedures.

Production of Large-Scale Arrays
Serial ribbons of 100-nm-thick sections were cut with a jumbo ultra diamond knife (Diatome) and collected onto gelatin-coated coverslips; typical arrays contained ~1,500–2,000 serial sections. Coverslips were incubated with 50 mM glycine in Tris buffered saline, blocked with 5% normal goat serum and 0.05% Tween-20, and incubated with the following primary antibodies: chicken anti-GFP (RRID: AB_300798; 1:2,500; Abcam), mouse anti-FLAG M2 (RRID: AB_259529; 1:2,500; Sigma), and guinea pig anti-synaptophysin1 (RRID: AB_1210382; 1:2,500; Synaptic Systems). The coverslips were then incubated with the following secondary antibodies: goat anti-guinea pig, 647 nm; goat anti-mouse, 555 nm; and goat anti-chicken, 488 nm (Jackson ImmunoResearch and Life Technologies). Registered and aligned large-volume arrays will be deposited to http://neurodata.io/projects/bloss16/.

Array Imaging
Arrays were imaged similar to Rah et al. (2013). Sixteen-bit images with isotropic voxels (x-y-z dimensions are as follows: 100 nm × 100 nm × 100 nm) were acquired using a Zeiss AxioObserver widefield epifluorescence microscope equipped with a 63×, 1.4 NA oil-immersion objective, custom-built array acquisition software, and an infrared skew-beam autofocus system. See Supplemental Experimental Procedures.

Synapse Analysis
EGFP+ dendrites, along with the corresponding region of interest in the FLAG and Syn1 channels, were segmented into binary masks using intensity-based thresholds. Because of the large signal-to-noise ratio of each channel (5- to 10-fold intensity change), the identification of triple-labeled synapses was relatively invariant to modest changes in the intensity threshold (see Supplemental Experimental Procedures for quantification).

For the correlative AT-TEM analysis, putative synapses were identified first by analyzing the FLAG and EGFP channels (i.e., in the absence of the

thresholded Syn1 signal), followed by examination of the corresponding TEM ultrastructure. In TEM micrographs, structures were considered inhibitory synapses if they met strict criteria for symmetric synapses (see Supplemental Experimental Procedures). After TEM analysis, the array images were re-examined, this time with the Syn1 mask visible, and putative array synaptic contacts were classified as blind to the TEM characterization. See Supplemental Experimental Procedures.

Computational Modeling

For performing simulations, two complete CA1 pyramidal neuron morphologies were reconstructed. All simulations were performed using the NEURON simulation software (Hines and Carnevale, 1997) with a variable time step. Code for the simulations has been deposited to our laboratory website (www.janelia.org/lab/spruston-lab/resources) and the ModelDB database (https://senselab.med.yale.edu/modeldb/). See Supplemental Experimental Procedures.

Statistical Analysis

All statistical results are reported in table form in the Supplemental Information. Correlations were performed using two-tailed Pearson correlations. Deviations between the expected and actual synapse numbers for each branch were examined with Monte Carlo simulations. Differences between the number and density of synapses on branch types were examined with two-tailed Student's t tests or one-way ANOVAs followed by Bonferroni post hoc tests. Differences between the synaptic densities at the sub-branch level were tested using one-way ANOVA with Bonferroni post hoc tests. All data presented in the figures have been deposited to our laboratory website (http://www.janelia.org/lab/spruston-lab/resources) and Figshare (http://dx.doi.org/10.6084/m9.figshare.2055774 and http://dx.doi.org/10.6084/m9.figshare.2055753). See Supplemental Experimental Procedures.

SUPPLEMENTAL INFORMATION

Supplemental Information includes Supplemental Experimental Procedures, six figures, seven tables, and two movies and can be found with this article online at http://dx.doi.org/10.1016/j.neuron.2016.01.029.

REFERENCES

Andrasfalvy, B.K., and Magee, J.C. (2001). Distance-dependent increase in AMPA receptor number in the dendrites of adult hippocampal CA1 pyramidal neurons. J. Neurosci. 21, 9151–9159.

Bar-Ilan, L., Gidon, A., and Segev, I. (2012). The role of dendritic inhibition in shaping the plasticity of excitatory synapses. Front. Neural Circuits 6, 118.

Bezaire, M.J., and Soltesz, I. (2013). Quantitative assessment of CA1 local circuits: knowledge base for interneuron-pyramidal cell connectivity. Hippocampus 23, 751–785.

Branco, T., and Häusser, M. (2010). The single dendritic branch as a fundamental functional unit in the nervous system. Curr. Opin. Neurobiol. 20, 494–502.

Brown, S.P., and Hestrin, S. (2009). Intracortical circuits of pyramidal neurons reflect their long-range axonal targets. Nature 457, 1133–1136.

Buhl, E.H., Szilágyi, T., Halasy, K., and Somogyi, P. (1996). Physiological properties of anatomically identified basket and bistratified cells in the CA1 area of the rat hippocampus in vitro. Hippocampus 6, 294–305.

Collman, F., Buchanan, J., Phend, K.D., Micheva, K.D., Weinberg, R.J., and Smith, S.J. (2015). Mapping synapses by conjugate light-electron array tomography. J. Neurosci. 35, 5792–5807.

Druckmann, S., Feng, L., Lee, B., Yook, C., Zhao, T., Magee, J.C., and Kim, J. (2014). Structured synaptic connectivity between hippocampal regions. Neuron 81, 629–640.

Elfant, D., Pál, B.Z., Emptage, N., and Capogna, M. (2008). Specific inhibitory synapses shift the balance from feedforward to feedback inhibition of hippocampal CA1 pyramidal cells. Eur. J. Neurosci. 27, 104–113.

Feng, G., Mellor, R.H., Bernstein, M., Keller-Peck, C., Nguyen, Q.T., Wallace, M., Nerbonne, J.M., Lichtman, J.W., and Sanes, J.R. (2000). Imaging neuronal subsets in transgenic mice expressing multiple spectral variants of GFP. Neuron 28, 41–51.

Fuentealba, P., Begum, R., Capogna, M., Jinno, S., Márton, L.F., Csicsvari, J., Thomson, A., Somogyi, P., and Klausberger, T. (2008). Ivy cells: a population of nitric-oxide-producing, slow-spiking GABAergic neurons and their involvement in hippocampal network activity. Neuron 57, 917–929.

Fuentealba, P., Klausberger, T., Karayannis, T., Suen, W.Y., Huck, J., Tomioka, R., Rockland, K., Capogna, M., Studer, M., Morales, M., and Somogyi, P. (2010). Expression of COUP-TFII nuclear receptor in restricted GABAergic neuronal populations in the adult rat hippocampus. J. Neurosci. 30, 1595–1609.

Gentet, L.J., Kremer, Y., Taniguchi, H., Huang, Z.J., Staiger, J.F., and Petersen, C.C. (2012). Unique functional properties of somatostatin-expressing GABAergic neurons in mouse barrel cortex. Nat. Neurosci. 15, 607–612.

Gidon, A., and Segev, I. (2012). Principles governing the operation of synaptic inhibition in dendrites. Neuron 75, 330–341.

Golding, N.L., Staff, N.P., and Spruston, N. (2002). Dendritic spikes as a mechanism for cooperative long-term potentiation. Nature 418, 326–331.

Halasy, K., Buhl, E.H., Lörinczi, Z., Tamás, G., and Somogyi, P. (1996). Synaptic target selectivity and input of GABAergic basket and bistratified interneurons in the CA1 area of the rat hippocampus. Hippocampus 6, 306–329.

Hao, J., Wang, X.D., Dan, Y., Poo, M.M., and Zhang, X.H. (2009). An arithmetic rule for spatial summation of excitatory and inhibitory inputs in pyramidal neurons. Proc. Natl. Acad. Sci. USA 106, 21906–21911.

Hines, M.L., and Carnevale, N.T. (1997). The NEURON simulation environment. Neural Comput. 9, 1179–1209.

Hippenmeyer, S., Vrieseling, E., Sigrist, M., Portmann, T., Laengle, C., Ladle, D.R., and Arber, S. (2005). A developmental switch in the response of DRG neurons to ETS transcription factor signaling. PLoS Biol. 3, e159.

Jadi, M., Polsky, A., Schiller, J., and Mel, B.W. (2012). Location-dependent effects of inhibition on local spiking in pyramidal neuron dendrites. PLoS Comput. Biol. 8, e1002550.

Jadi, M.P., Behabadi, B.F., Poleg-Polsky, A., Schiller, J., and Mel, B.W. (2014). An augmented two-layer model captures nonlinear analog spatial integration effects in pyramidal neuron dendrites. Proc IEEE Inst Electr Electron Eng 102, 782–798.

Jarsky, T., Roxin, A., Kath, W.L., and Spruston, N. (2005). Conditional dendritic spike propagation following distal synaptic activation of hippocampal CA1 pyramidal neurons. Nat. Neurosci. 8, 1667–1676.

Katona, I., Acsády, L., and Freund, T.F. (1999). Postsynaptic targets of somatostatin-immunoreactive interneurons in the rat hippocampus. Neuroscience 88, 37–55.

Katz, Y., Menon, V., Nicholson, D.A., Geinisman, Y., Kath, W.L., and Spruston, N. (2009). Synapse distribution suggests a two-stage model of dendritic integration in CA1 pyramidal neurons. Neuron 63, 171–177.

Kim, Y., Hsu, C.L., Cembrowski, M.S., Mensh, B.D., and Spruston, N. (2015). Dendritic sodium spikes are required for long-term potentiation at distal synapses on hippocampal pyramidal neurons. eLife 4, 4.

Klausberger, T. (2009). GABAergic interneurons targeting dendrites of pyramidal cells in the CA1 area of the hippocampus. Eur. J. Neurosci. 30, 947–957.

Klausberger, T., and Somogyi, P. (2008). Neuronal diversity and temporal dynamics: the unity of hippocampal circuit operations. Science 321, 53–57.

Klausberger, T., Márton, L.F., Baude, A., Roberts, J.D., Magill, P.J., and Somogyi, P. (2004). Spike timing of dendrite-targeting bistratified cells during hippocampal network oscillations in vivo. Nat. Neurosci. 7, 41–47.

Kleindienst, T., Winnubst, J., Roth-Alpermann, C., Bonhoeffer, T., and Lohmann, C. (2011). Activity-dependent clustering of functional synaptic inputs on developing hippocampal dendrites. Neuron 72, 1012–1024.

Koch, C., Poggio, T., and Torre, V. (1983). Nonlinear interactions in a dendritic tree: localization, timing, and role in information processing. Proc. Natl. Acad. Sci. USA 80, 2799–2802.

Kvitsiani, D., Ranade, S., Hangya, B., Taniguchi, H., Huang, J.Z., and Kepecs, A. (2013). Distinct behavioural and network correlates of two interneuron types in prefrontal cortex. Nature 498, 363–366.

Lapray, D., Lasztoczi, B., Lagler, M., Viney, T.J., Katona, L., Valenti, O., Hartwich, K., Borhegyi, Z., Somogyi, P., and Klausberger, T. (2012). Behavior-dependent specialization of identified hippocampal interneurons. Nat. Neurosci. 15, 1265–1271.

Losonczy, A., Makara, J.K., and Magee, J.C. (2008). Compartmentalized dendritic plasticity and input feature storage in neurons. Nature 452, 436–441.

Lovett-Barron, M., Turi, G.F., Kaifosh, P., Lee, P.H., Bolze, F., Sun, X.H., Nicoud, J.F., Zemelman, B.V., Sternson, S.M., and Losonczy, A. (2012). Regulation of neuronal input transformations by tunable dendritic inhibition. Nat. Neurosci. 15, 423–430, S1–S3.

Lovett-Barron, M., Kaifosh, P., Kheirbek, M.A., Danielson, N., Zaremba, J.D., Reardon, T.R., Turi, G.F., Hen, R., Zemelman, B.V., and Losonczy, A. (2014). Dendritic inhibition in the hippocampus supports fear learning. Science 343, 857–863.

Maccaferri, G., Roberts, J.D., Szucs, P., Cottingham, C.A., and Somogyi, P. (2000). Cell surface domain specific postsynaptic currents evoked by identified GABAergic neurones in rat hippocampus in vitro. J. Physiol. 524, 91–116.

Megías, M., Emri, Z., Freund, T.F., and Gulyás, A.I. (2001). Total number and distribution of inhibitory and excitatory synapses on hippocampal CA1 pyramidal cells. Neuroscience 102, 527–540.

Micheva, K.D., and Smith, S.J. (2007). Array tomography: a new tool for imaging the molecular architecture and ultrastructure of neural circuits. Neuron 55, 25–36.

Milstein, A.D., Bloss, E.B., Apostolides, P.F., Vaidya, S.P., Dilly, G.A., Zemelman, B.V., and Magee, J.C. (2015). Inhibitory Gating of Input Comparison in the CA1 Microcircuit. Neuron 87, 1274–1289.

Müller, C., Beck, H., Coulter, D., and Remy, S. (2012). Inhibitory control of linear and supralinear dendritic excitation in CA1 pyramidal neurons. Neuron 75, 851–864.

Müllner, F.E., Wierenga, C.J., and Bonhoeffer, T. (2015). Precision of inhibition: dendritic inhibition by individual GABAergic synapses on hippocampal pyramidal cells is confined in space and time. Neuron 87, 576–589.

Nicholson, D.A., Trana, R., Katz, Y., Kath, W.L., Spruston, N., and Geinisman, Y. (2006). Distance-dependent differences in synapse number and AMPA receptor expression in hippocampal CA1 pyramidal neurons. Neuron 50, 431–442.

Oláh, S., Füle, M., Komlósi, G., Varga, C., Báldi, R., Barzó, P., and Tamás, G. (2009). Regulation of cortical microcircuits by unitary GABA-mediated volume transmission. Nature 461, 1278–1281.

Petreanu, L., Mao, T., Sternson, S.M., and Svoboda, K. (2009). The subcellular organization of neocortical excitatory connections. Nature 457, 1142–1145.

Pfeffer, C.K., Xue, M., He, M., Huang, Z.J., and Scanziani, M. (2013). Inhibition of inhibition in visual cortex: the logic of connections between molecularly distinct interneurons. Nat. Neurosci. 16, 1068–1076.

Pi, H.J., Hangya, B., Kvitsiani, D., Sanders, J.I., Huang, Z.J., and Kepecs, A. (2013). Cortical interneurons that specialize in disinhibitory control. Nature 503, 521–524.

Price, C.J., Cauli, B., Kovacs, E.R., Kulik, A., Lambolez, B., Shigemoto, R., and Capogna, M. (2005). Neurogliaform neurons form a novel inhibitory network in the hippocampal CA1 area. J. Neurosci. 25, 6775–6786.

Rah, J.C., Bas, E., Colonell, J., Mishchenko, Y., Karsh, B., Fetter, R.D., Myers, E.W., Chklovskii, D.B., Svoboda, K., Harris, T.D., and Isaac, J.T. (2013). Thalamocortical input onto layer 5 pyramidal neurons measured using quantitative large-scale array tomography. Front. Neural Circuits 7, 177.

Royer, S., Zemelman, B.V., Losonczy, A., Kim, J., Chance, F., Magee, J.C., and Buzsáki, G. (2012). Control of timing, rate and bursts of hippocampal place cells by dendritic and somatic inhibition. Nat. Neurosci. 15, 769–775.

Schoonover, C.E., Tapia, J.C., Schilling, V.C., Wimmer, V., Blazeski, R., Zhang, W., Mason, C.A., and Bruno, R.M. (2014). Comparative strength and dendritic organization of thalamocortical and corticocortical synapses onto excitatory layer 4 neurons. J. Neurosci. 34, 6746–6758.

Spruston, N. (2008). Pyramidal neurons: dendritic structure and synaptic integration. Nat. Rev. Neurosci. 9, 206–221.

Spruston, N., Schiller, Y., Stuart, G., and Sakmann, B. (1995). Activity-dependent action potential invasion and calcium influx into hippocampal CA1 dendrites. Science 268, 297–300.

Suloway, C., Pulokas, J., Fellmann, D., Cheng, A., Guerra, F., Quispe, J., Stagg, S., Potter, C.S., and Carragher, B. (2005). Automated molecular microscopy: the new Leginon system. J. Struct. Biol. 151, 41–60.

Szabadics, J., Tamás, G., and Soltesz, I. (2007). Different transmitter transients underlie presynaptic cell type specificity of GABAA,slow and GABAA,fast. Proc. Natl. Acad. Sci. USA 104, 14831–14836.

Takahashi, N., Kitamura, K., Matsuo, N., Mayford, M., Kano, M., Matsuki, N., and Ikegaya, Y. (2012). Locally synchronized synaptic inputs. Science 335, 353–356.

Taniguchi, H., He, M., Wu, P., Kim, S., Paik, R., Sugino, K., Kvitsiani, D., Fu, Y., Lu, J., Lin, Y., et al. (2011). A resource of Cre driver lines for genetic targeting of GABAergic neurons in cerebral cortex. Neuron 71, 995–1013.

Tricoire, L., Pelkey, K.A., Daw, M.I., Sousa, V.H., Miyoshi, G., Jeffries, B., Cauli, B., Fishell, G., and McBain, C.J. (2010). Common origins of hippocampal Ivy and nitric oxide synthase expressing neurogliaform cells. J. Neurosci. 30, 2165–2176.

Viswanathan, S., Williams, M.E., Bloss, E.B., Stasevich, T.J., Speer, C.M., Nern, A., Pfeiffer, B.D., Hooks, B.M., Li, W.P., English, B.P., et al. (2015). High-performance probes for light and electron microscopy. Nat. Methods 12, 568–576.

Vong, L., Ye, C., Yang, Z., Choi, B., Chua, S., Jr., and Lowell, B.B. (2011). Leptin action on GABAergic neurons prevents obesity and reduces inhibitory tone to POMC neurons. Neuron 71, 142–154.

Watanabe, S., Lehmann, M., Hujber, E., Fetter, R.D., Richards, J., Söhl-Kielczynski, B., Felies, A., Rosenmund, C., Schmoranzer, J., and Jorgensen, E.M. (2014). Nanometer-resolution fluorescence electron microscopy (nano-EM) in cultured cells. Methods Mol. Biol. 1117, 503–526.

Yoshimura, Y., and Callaway, E.M. (2005). Fine-scale specificity of cortical networks depends on inhibitory cell type and connectivity. Nat. Neurosci. 8, 1552–1559.